Surface & Coatings Technology 231 (2013) 219–223

Contents lists available at ScienceDirect

Surface & Coatings Technology

journal homepage: www.elsevier.com/locate/surfcoat

A characterization on emission property of In_2O_3–SiO_2 nanocomposite thin films

Yang-Ru Lyu, Tsung-Eong Hsieh *

Department of Materials Science and Engineering, National Chiao Tung University, Hsinchu, 30010, Taiwan, ROC

ARTICLE INFO

Available online 18 June 2012

Keywords:
In_2O_3
Nanocomposite
Photoluminescence
Emission mechanisms

ABSTRACT

Nanocomposite thin films containing finely dispersed, crystalline In_2O_3 nanoparticles embedded in SiO_2 matrix were fabricated by target-attachment sputtering method. Transmission electron microscopy observed single crystalline In_2O_3 nanoparticles uniformly embedded in SiO_2 matrix of the samples with In_2O_3 content less than about 60 vol.%. Photoluminescence spectra of the In_2O_3–SiO_2 nanocomposite samples were found to comprise of the blue, green and red emissions. Analytical results indicated that the red and green emissions are correlated to the transitions from conduction band (CB) edge to the $In_i^{\bullet\bullet\bullet}$ and V'''_{In} defect levels, respectively, while the blue emission is originated from the transition from CB edge to $V_O^{\bullet\bullet}$ level or from $V_O^{\bullet}$ level to the valence band edge.

1. Introduction

As a well-known wide bandgap (E_g) semiconductor, indium oxide (In_2O_3; $E_g = 3.75$ eV) recently attracts numerous attentions in optoelectronic applications owing to its high electrical conductivity and high transparency in visible-light wavelength range [1,2]. One of the attractive properties of In_2O_3 is its strong visible-light photoluminescence (PL). Lee et al. reported the PL signal at 637 nm from the In_2O_3 thin films [3]. Mazzera et al. observed three emission bands separately located at 454, 563 and 631 nm in the cathodoluminescence spectra of In_2O_3 samples [4]. The correlation of In_2O_3 emissions to oxygen vacancy has been separately discussed by Liang et al. [5] and Ko et al. [6]. They ascribed the emissions in the blue-green and blue-red regions to the presence of oxygen vacancies in In_2O_3. Furthermore, broad PL peaks at 416 and 435 nm from In_2O_3 nanowires were observed by Wu et al. [7]. Guha et al. found a blue-green PL emission in the In_2O_3 nanopyramid and nanocolumn samples [8]. Their studies also reported the correlations of luminescence property to oxygen defects in In_2O_3.

Strong UV emission that resulted from the direct bandgap transition in In_2O_3 has been reported by Murali et al. [9] and Seo et al. [10], respectively. However, the correlation of emissions to the transitions in between the defect levels of In_2O_3-based samples remains obscure since the experimental data rarely illustrated the defect-level transitions in a straightforward manner. As reported previously [5–8], a wide range of emissions in visible-light wavelength range has been ascribed to the oxygen vacancies in In_2O_3. This might be inappropriate since the oxygen defect levels unlikely split in such a wide range in the bandgap of In_2O_3. As a result, a clarification on the emission mechanisms corresponding to the defect-level transitions in In_2O_3 is required.

This work prepares the nanocomposite thin films comprised of In_2O_3 nanoparticles embedded in SiO_2 matrix by utilizing the target-attachment sputtering method [11,12]. Characterizations of PL emissions, microstructures and compositions of the nanocomposite samples containing various sizes and amounts of In_2O_3 nanoparticles are presented. Accordingly, the PL properties correlated to the defect-level transitions of emissions in nanocomposite thin films containing In_2O_3 nanoparticles are discussed.

2. Experimental details

The In_2O_3–SiO_2 nanocomposite thin films were deposited on Si wafer substrates by the target-attachment method in a sputtering system with the background pressure better than 10^{-7} Torr. Appropriate amounts of In_2O_3 pellets were mounted on a 3-inch quartz target and the radio-frequency (RF) magnetron sputtering deposition was carried out at the working pressure of 3.5 mTorr with argon (Ar) as the inlet gas flow. The sizes and densities of In_2O_3 nanoparticles in the nanocomposite thin films were adjusted by varying the sputtering power and the number of In_2O_3 pellets. Table 1 lists the sample designation established in terms of the sputtering deposition conditions. Characterizations of PL emissions, microstructures and compositions of the samples were immediately followed after the completion of sample preparation without performing the post annealing treatment. PL spectra were measured at room temperature in the wavelength range of 350 to 750 nm using a self-assembly PL apparatus equipped with a 325 nm He–Cd laser. Microstructures of nanocomposite thin films were characterized by transmission electron microscopy (TEM; JEOL JEM-2100F) operating at 200 kV. Evolution of chemical bonds in the samples was examined by *X*-ray photoemission spectroscopy (XPS; American Physical Electronics ESCA PHI 1600) using the Mg-K_α *X*-ray excitation.

* Corresponding author. Tel.: +886 3 5712121x55306; fax: +886 3 5724727.
E-mail address: tehsieh@mail.nctu.edu.tw (T-E. Hsieh).

0257-8972/$ – see front matter © 2012 Elsevier B.V. All rights reserved.
doi:10.1016/j.surfcoat.2012.06.037

Table 1
A list of In_2O_3 nanoparticle sizes, In_2O_3 contents and sputtering deposition conditions of nanocomposite samples.

Sample designation	Particle size (nm)	In_2O_3 content (vol. %)	Sputtering deposition condition	
			RF power (W)	Pellet area coverage ration (%)
a	4.4	11.35	100	5
b	4.78	11.87	130	5
c	5.02	12.54	160	5
d	4.71	57.47	100	15
e	4.8	57.55	130	15
f	4.97	57.57	160	15
g	4.9	81.80	70	25
h	4.92	81.83	100	25

3. Results and discussion

3.1. Microstructure characterization

Fig. 1(a)–(e) presents the TEM micrographs of various In_2O_3–SiO_2 nanocomposite thin films prepared in this study. Attached in the upper right-hand corners of Fig. 1(a)–(c) are the enlarged images of In_2O_3 nanoparticles embedded in those nanocomposite samples. The lattice fringes decorating in the In_2O_3 nanoparticles indicate that each of them corresponds to a single crystalline particle. However, those lattice fringes became difficult to be observed in samples *g* and *i* (Fig. 1(d) and (e)) due to their high In_2O_3 contents that the images of nanoparticles severely overlap when projected on the TEM screen. Representative selected area electron diffraction (SAED) of sample shown in Fig. 1(f) indicates that the embedded In_2O_3 phase is body-centered-cubic (BCC) structure according to the Joint Committee of Powder Diffraction Standards (JCPDS) No. 06-0416. The average particle sizes were obtained by measuring the sizes of at least 60 In_2O_3 nanoparticles in the TEM images for each of the samples and the results are summarized in Table 1.

3.2. XPS analysis

Fig. 2(a) depicts the In 3*d* XPS spectra of nanocomposite samples which indicate that all samples contain the sole In_2O_3 phase without the presence of metallic In (443.56 eV [13]). A monotonic increase in intensities of In 3*d* XPS peaks can be observed in samples *a* to *j* with the increase of In_2O_3 pellet-to-target area coverage ratio and RF sputtering power. Moreover, the binding energies corresponding to In $3d_{3/2}$ and In $3d_{5/2}$ XPS peaks shown in Fig. 2(a) are separately equal to 452.43 ± 0.10 eV and 444.83 ± 0.10 eV, which are in agreement with the reported values for In – O bond [14]. We note that XPS spectra shown in Fig. 2(a) were also adopted to calibrate the In_2O_3 contents in the samples and the results were presented in terms of the volume ratios of In_2O_3 in the samples as listed in Table 1.

The O 1*s* XPS spectra shown in Fig. 2(b) reveal, with the increase of In_2O_3 pellet-to-target area coverage ratio and RF sputtering power, the XPS peak shifts toward the high binding energy side and the asymmetries of XPS peaks become apparent for the samples with high In_2O_3 contents. According to Dupin et al. [15], the status of oxygen defects in oxide systems could be distinguished by analyzing the O 1*s* XPS profiles. With the aid of the de-convolution of XPS spectra, the roles of various oxygen defects in the shift and asymmetry of O 1*s* XPS profiles shown in Fig. 2(b) can be clarified.

Curve fitting results of O 1*s* XPS spectra for samples are summarized in Table 2. Three different oxygen defect species present in the nanocomposite samples: $O_{lattice}$, O^-, and O^{2-} separately represent the lattice oxygen in In_2O_3 lattice (~530.2 eV), the oxygen ions at the nanoparticle surface (~531.8 eV), and the loosely bound oxygen in the amorphous SiO_2 or partially weakly adsorbed oxygen species (~532.7 eV) [11]. The O^- ions were generated on nanoparticle surface during the sputtering as reported by Chen et al. [16]. Moreover, the content of $O_{lattice}$ component increases from 5.91 to 14.36% for samples *a* to *j*. This is ascribed to the increases of In_2O_3 content in nanocomposite layer since the $O_{lattice}$ signal is correlated to the In – O bond. Note that the variation of $O_{lattice}$ component deduced from XPS profiles allows us to estimate the deviation of stoichiometric ratio for In_2O_3 phase in each of the samples. The results obtained will be discussed in conjunction of the PL properties to identify the emission mechanism of In_2O_3.

3.3. Photoluminance property and origins of emissions

Fig. 3 presents the PL spectra of nanocomposite samples *a*–*j*. We note that the PL intensity decreases with the increase of In_2O_3 content of the sample. According to the TEM images shown in Fig. 1(d) and (e), high In_2O_3 content results in the coalescence of nanoparticles and, hence, the luminescence property of such nanocomposite thin films becomes a resemblance to that of In_2O_3 bulk which is known to emit no visible light at room temperature [17]. All PL spectra can be de-convoluted into red, green and blue emissions; the peak positions and integrated intensity ratios of emissions deduced from the PL curve fitting results are summarized in Table 2. Since $E_g = 3.75$ eV (~330 nm) for In_2O_3 which is located at the UV regime, those de-convoluted PL emissions were hence correlated to the carrier recombination in between the conduction band (CB) edge and the defect levels and/or the defect levels and the valence band (VB) edge. Moreover, although there were slight shifts of emission peaks due to weak confinement effect, the quantum confinement effect on PL property is negligible since the sizes of In_2O_3 nanoparticles prepared in this study are larger than the Bohr radius of In_2O_3 (= 2.14 nm) [5]. As a result, the PL data presented in this study are appropriate for characterizing the mechanisms of visible-light emissions of In_2O_3–SiO_2 nanocomposite thin films.

Previous studies reported several possible defect types in In_2O_3, *e.g.*, oxygen vacancy ($V_O^{\bullet\bullet}$), indium interstitial ($In_i^{\bullet\bullet\bullet}$) and indium vacancy ($V'''_{In}$) [4,10]. Due to its relatively large size (0.138 nm), oxygen interstitial (O''_i) is unlikely present in our samples and hence it is aborted in the following discussion [4]. Correlations of visible-light emissions to interface features of the samples have been reported in several systems containing wide-bandgap semiconductors [18–22] and strong emission was observed in the nanocomposite samples with high specific-surface-area (SSA) properties. Fig. 4(a) presents the normalized integrated intensities of the blue, green and red emissions as a function of the surface-to-volume ratio and particle radius of In_2O_3 nanoparticles. It was found that the intensity ratios of blue and red emissions decrease with the increase of surface-to-volume ratio and *vice versa* for green emission. This indicates that those emissions may result from different carrier recombination processes in nanocomposite samples. It is well known that, with the shrinkage of particle size, the band bending effects at the particle surface become obvious [23,24]. Accordingly, the surface states are created due to the holes migrating toward the particle surface while the volume states are generated owing to the electron migrating into the bulk of particle. According to trends depicted in Fig. 4(a), it can be concluded that the red and blue emissions are associated with the donor defects whereas the green emission is correlated to the acceptor defects in In_2O_3 nanoparticles. For $In_i^{\bullet\bullet\bullet}$, it should act as a donor level more close to CB edge in comparison with $V_O^{\bullet\bullet}$ and, hence, the transition from CB edge to $In_i^{\bullet\bullet\bullet}$ defect level is most likely correlated to the red emission. This is in agreement with that reported by Kumar et al. who proposed that the presence of $In_i^{\bullet\bullet\bullet}$ in In_2O_3 is responsible to the red emission [25].

As to the green and blue emissions, they are commonly related to the presence of oxygen deficiencies in the samples [7,10,26]. Nevertheless,

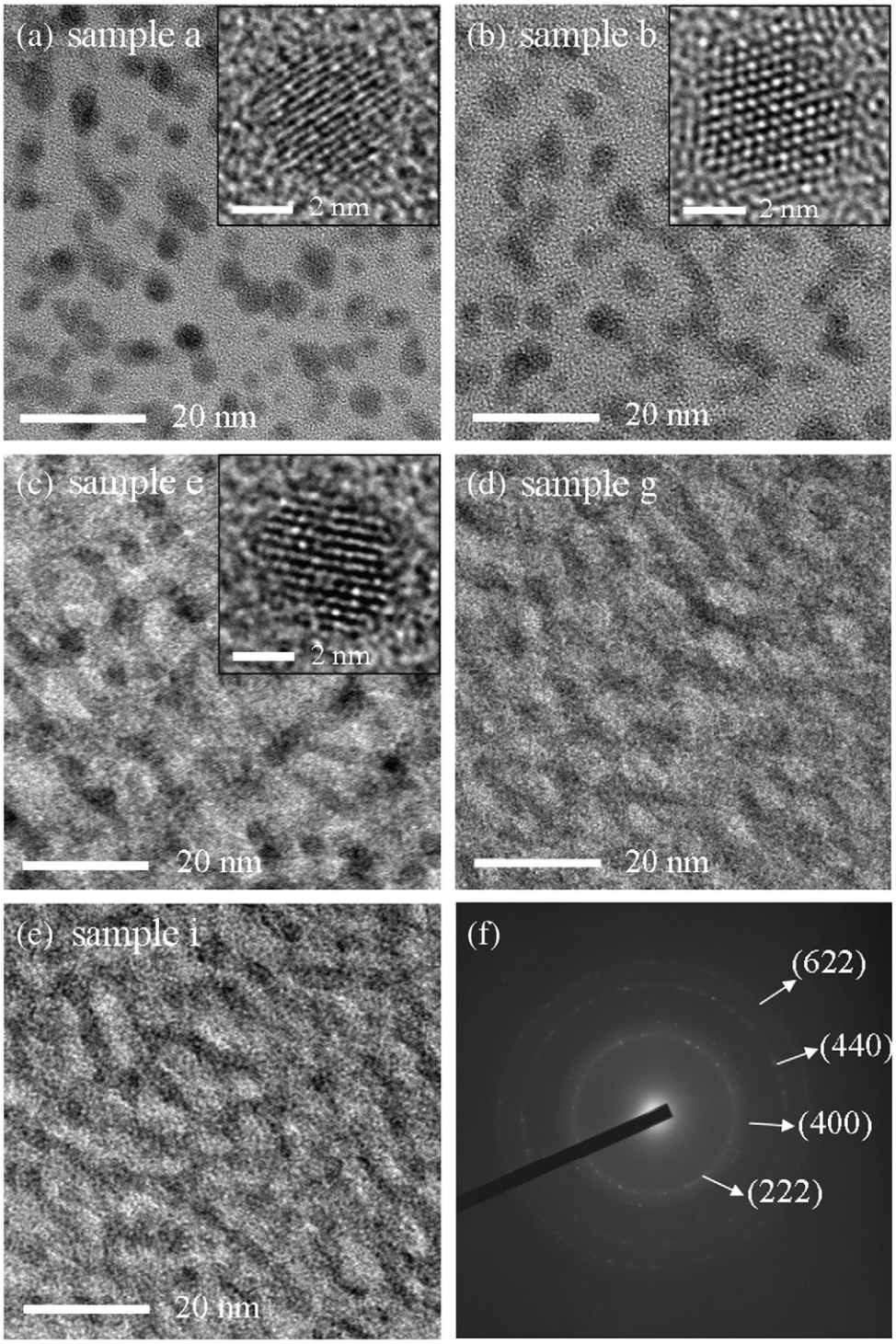

Fig. 1. (a) to (e) show the TEM micrographs corresponding to samples *a*, *b*, *e*, *g* and *i*. Attached at the upper right-hand corners of (a) to (c) are the high-magnification images of In_2O_3 nanoparticles. (f) is a typical SAED pattern taken from the nanocomposite sample.

experimental evidences to verify such a correlation remain insufficient [27,28]. For instance, Wu et al. ascribed the green emission of In_2O_3 to the oxygen vacancies (V_O^X) and In – O vacancy complex $(V_{In},V_O)^X$ [7]. However, the shallow donor level generated by V_O^X is not well identified. The plots shown in Fig. 4(a) indicate that the green and blue emissions are separately related to the acceptor defect level and the donor defect level. Among the possible acceptor defects in In_2O_3, *i.e.*, V'_{In}, V''_{In} and V'''_{In}, the green emission is hence correlated to the transition from CB edge or shallow donor levels to the V'''_{In} since it is a plausible defect type in In_2O_3 in accord with the Frenkel disorder reaction $In_{In} \rightarrow In_i^{\bullet\bullet\bullet} + V'''_{In}$.

Blue emission is another visible emission that has been attributed to the presence of oxygen defects in the samples [5,6]. Fig. 4(a) indicates, similarly to the red emission, such an emission also relies on the transition relating to donor levels in the samples. According to relative amounts of $O_{lattice}$ component deduced from XPS profiles, we calculated the deviations of stoichiometry for In_2O_3 (*i.e.*, In:O = 2:3) in order to estimate the amount of oxygen defects in In_2O_3 nanoparticles of various

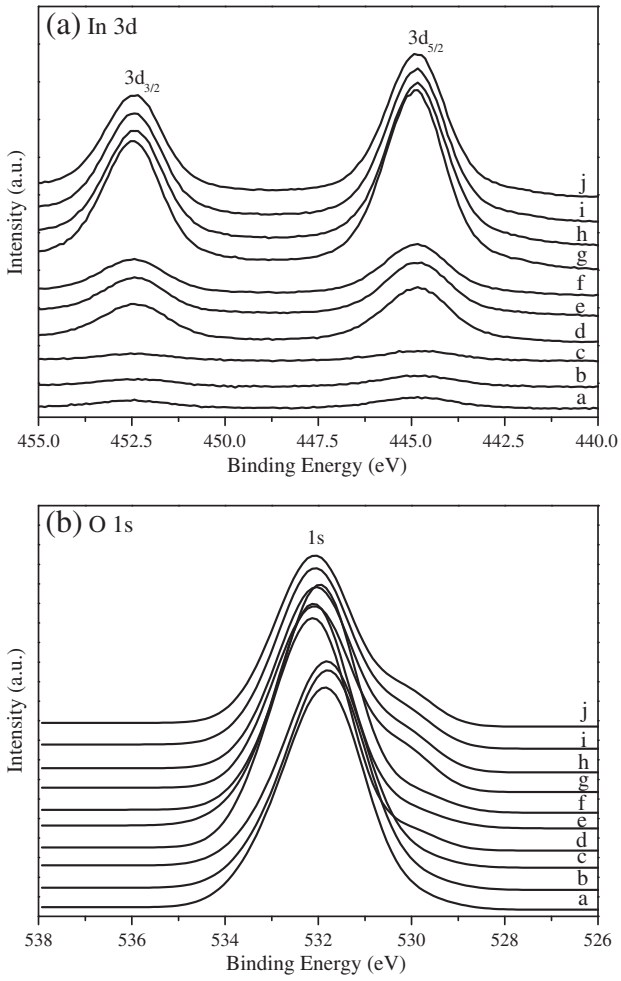

Fig. 2. (a) In 3*d* and (b) O 1*s* XPS spectra of In_2O_3–SiO_2 nanocomposite samples.

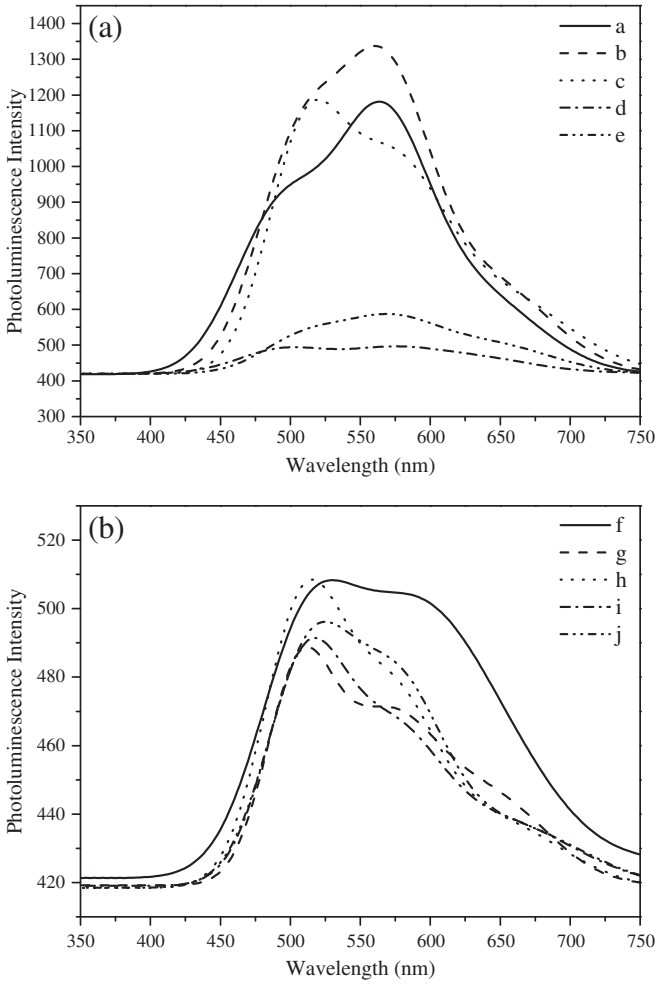

Fig. 3. PL spectra of In_2O_3–SiO_2 nanocomposite samples (a) *a*–*e* and (b) *f*–*j*.

samples. Fig. 4(b) plots the normalized integrated intensity of blue emission against the deviation of stoichiometry for In_2O_3 nanoparticles. Apparently, the increase of non-stoichiometry in In_2O_3 amplifies the blue emission, illustrating that the presence of oxygen defects in In_2O_3 nanoparticles is highly correlated to such an emission. However, oxygen defects include singly ionized $V_O^{\bullet}$ and doubly ionized $V_O^{\bullet\bullet}$ in many oxides. Electron paramagnetic resonance (EPR) analysis on In_2O_3 [4,25] and several previous studies [29,30] have ascribed the blue emission to $V_O^{\bullet}$. Although $V_O^{\bullet\bullet}$ could not be detected due to its non-paramagnetic feature, $V_O^{\bullet\bullet}$ might form *via* the hole trapping process, *i.e.*, $V_O^{\bullet} + h \rightarrow V_O^{\bullet\bullet}$. Since the relative populations of $V_O^{\bullet}$ and $V_O^{\bullet\bullet}$ defects could not be distinguished in the present study, it is inferred that both the $V_O^{\bullet}$ and $V_O^{\bullet\bullet}$ donor levels are correlated to the blue emission. That is, in accord with the possible energy levels in bandgap diagram, the blue emission might result from the transition from CB edge to $V_O^{\bullet\bullet}$ level and/or the transition from $V_O^{\bullet}$ level and VB edge.

In accord with above discussions, the plausible defect energy levels corresponding to the red, green and blue emissions in bandgap diagram of In_2O_3 are constructed and delineated in Fig. 5. We hope that the analytical results presented in this study would benefit the

Table 2
Summary of XPS and PL curve fitting results for In_2O_3–SiO_2 nanocomposite samples and the integrated PL intensity ratios of visible-light emissions deduced from the PL curve fitting.

Sample designation	Binding energy (eV)			PL peak position (nm)			PL intensity ratio		
	$O_{lattice}$	O^- ion	O^{2-} ion	Red	Green	Blue	Red	Green	Blue
a	530.16	531.69	532.70	631.9	564.0	492.1	0.205	0.483	0.311
b	530.23	531.67	532.70	642.0	566.0	504.0	0.212	0.454	0.353
c	530.18	531.68	532.70	647.6	571.5	510.0	0.237	0.350	0.412
d	530.19	531.84	532.69	642.7	565.0	503.0	0.202	0.449	0.348
e	530.25	532.01	532.50	645.0	569.0	507.0	0.212	0.432	0.375
f	530.19	531.82	532.59	647.6	572.0	509.3	0.247	0.356	0.397
g	530.17	531.84	532.60	644.0	568.3	506.2	0.219	0.389	0.418
h	530.19	531.86	532.56	647.6	571.0	508.9	0.212	0.377	0.409
i	530.24	531.92	532.53	649.8	573.0	511.0	0.239	0.314	0.445
j	530.18	531.86	532.59	653.0	576.4	514.0	0.233	0.316	0.450

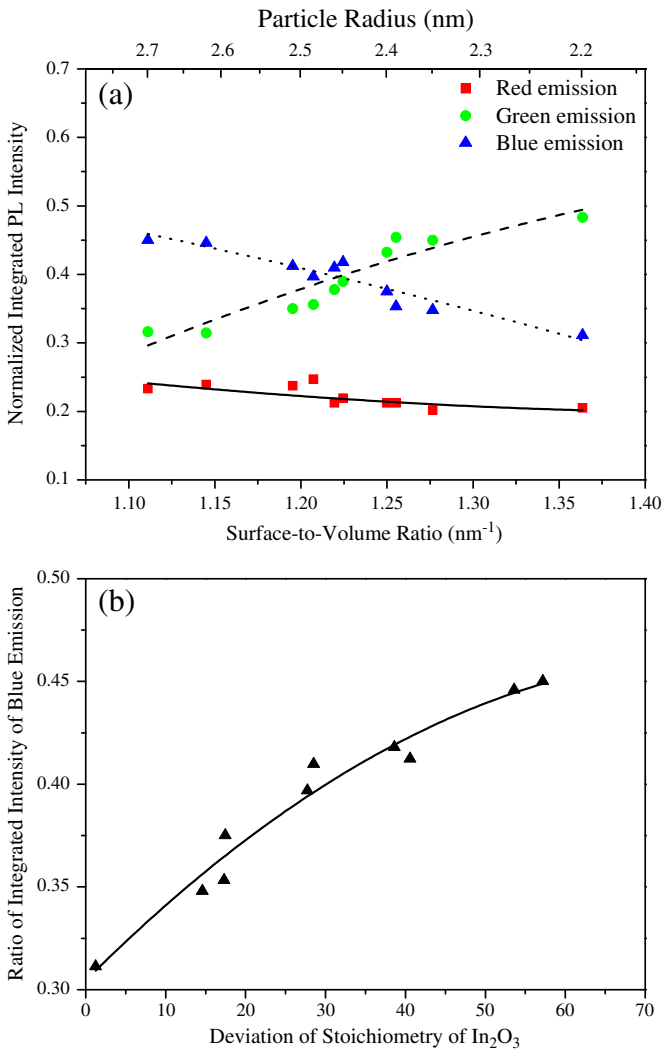

Fig. 4. Normalized integrated intensity of (a) visible-light emissions as a function of surface-to-volume ratio and sizes of In_2O_3 nanoparticles and (b) the ratio of integrated intensity of blue emission against the deviation of stoichiometry for In_2O_3.

understanding on the emission properties and their correlations to defect configuration of nano-scale In_2O_3.

4. Conclusions

The In_2O_3–SiO_2 nanocomposite films containing In_2O_3 nanoparticles were fabricated by target-attachment sputtering and their visible-light emission mechanisms were analyzed. Single crystalline In_2O_3 nanoparticles uniformly dispersed in SiO_2 matrix were observed by TEM in the samples with In_2O_3 content less than about 60 vol.%. XPS analysis revealed that the main oxygen defect type associated with In_2O_3 nanoparticles is the O^- ions residing on their surfaces due to the large SSA feature of nanoparticles. The PL spectra of the In_2O_3–SiO_2 nanocomposite thin films were found to comprise of blue, green, and red emissions. Since the direct bandgap transition of In_2O_3 is located at the UV regime and the quantum confinement effect is negligible in this study, those visible-light emissions are hence associated to the defect level transitions in bandgap of In_2O_3. In accord with the characterizations on luminance property, microstructures and composition of nanocomposite samples, the red emission is correlated with the transition from CB edge to $In_i^{\bullet\bullet\bullet}$ donor level, the green emission is originated from the transition from CB edge or shallow donor levels to the V'''_{In} acceptor level and the blue emission is resulted from the transition from CB edge to $V_O^{\bullet\bullet}$ level and/or the transition from $V_O^{\bullet}$ level and VB edge.

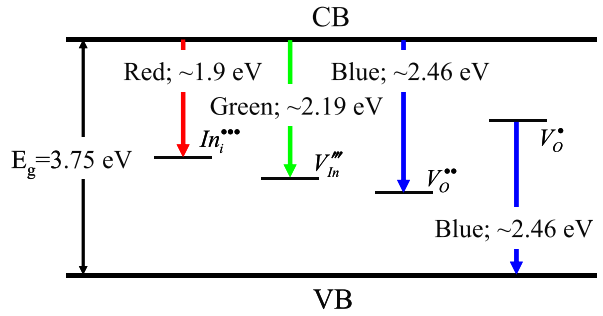

Fig. 5. Schematic illustration of bandgap diagram of In_2O_3 with the defect energy levels. The transitions corresponding to the red, green and blue emissions are indicated by the colored arrow lines in the plot.

Accordingly, the defect energy levels corresponding to the visible-light emissions in bandgap diagram of In_2O_3 was established in order to elucidate the luminance mechanisms of In_2O_3–SiO_2 nanocomposite thin films.

Acknowledgments

This work is supported by National Science Council (NSC), Taiwan, ROC, under the contract no. NSC98-2221-E-009-037-MY2. The assistance of TEM analysis provided by Mr. Wei-Lin Wang in the Department of Materials Science and Engineering, National Chiao Tung University, Taiwan, ROC, is also deeply acknowledged.

References

[1] R.A. Sailer, A. Wagner, C. Schmit, N. Klaverkamp, D.L. Schulz, Surf. Coat. Technol. 203 (2008) 835.
[2] Y. Shigesato, S. Takaki, T. Haranoh, J. Appl. Phys. 71 (1992) 3356.
[3] M.S. Lee, W.C. Choi, E.K. Kim, C.K. Kim, S.K. Min, Thin Solid Films 279 (1996) 1.
[4] M. Mazzera, M. Zha, D. Calestani, A. Zappettini, L. Lazzarini, G. Salviati, L. Zanotti, Nanotechnology 18 (2007) 355707.
[5] C.H. Liang, G.W. Meng, Y. Lei, F. Phillip, L.D. Zhang, Adv. Mater. 13 (2001) 1330.
[6] T.S. Ko, C.P. Chu, J.R. Chen, T.C. Lu, H.C. Kuo, S.C. Wang, J. Cryst. Growth 310 (2008) 2264.
[7] X.C. Wu, J.M. Hong, Z.J. Han, Y.R. Tao, Chem. Phys. Lett. 373 (2003) 28.
[8] P. Guha, S. Kar, S. Choudhari, Appl. Phys. Lett. 85 (2004) 3851.
[9] A. Murali, A. Barve, V.J. Leppert, S.H. Risbud, I.M. Kennedy, H.W.H. Lee, Nano Lett. 1 (2001) 287.
[10] W.S. Seo, H.H. Jo, K. Lee, J.T. Park, Adv. Mater. 15 (2003) 795.
[11] Y.Y. Peng, T.E. Hsieh, C.H. Hsu, Nanotechnology 16 (2005) 1.
[12] Y.Y. Peng, T.E. Hsieh, Appl. Phys. Lett. 89 (2006) 211909-1.
[13] R.W. Hewitt, N. Winograd, J. Appl. Phys. 51 (1980) 2620.
[14] A. Gurlo, M. Ivanovskaya, A. Pfau, U. Weimar, W. Gopel, Thin Solid Films 307 (1997) 288.
[15] J.C. Dupin, D. Gonbeau, P. Vinatier, A. Levasseur, Phys. Chem. Chem. Phys. 2 (2000) 1319.
[16] M. Chen, X. Wang, Y.H. Yu, Z.L. Pei, X.D. Bai, C. Sun, R.F. Huang, L.S. Wen, Appl. Surf. Sci. 158 (2000) 134.
[17] Y. Ohhata, F. Shinoki, S. Yoshida, Thin Solid Films 59 (1979) 255.
[18] S. Chakrabarti, D. Ganguli, S. Chaudhuri, J. Phys. D: Appl. Phys. 36 (2003) 146.
[19] L.I. Burova, D.I. Petukhov, A.A. Eliseev, A.V. Lukashin, Y.D. Tretyakov, Superlattices Microstruct. 39 (2006) 257.
[20] B. Damilano, N. Grandjean, F. Semond, J. Massies, M. Leroux, Appl. Phys. Lett. 75 (1999) 962.
[21] Y.G. Cao, X.L. Chen, Y.C. Lan, J.Y. Li, Y.P. Xu, T. Xu, Q.L. Liu, J.K. Liang, J. Cryst. Growth 213 (2000) 198.
[22] S.T. Selvan, C. Bullen, M. Ashokkumar, P. Mulvaney, Adv. Mater. 13 (2001) 985.
[23] Y.J. Lee, J.L. Gary, In: IEEE Photo. Spec. Conf., Hawaii, 1994, p. 287.
[24] H.H. Mueller, M.J. Schulz, IEEE Trans. Electron Devices 44 (1997) 1539.
[25] M. Kumar, V.N. Singh, F. Singh, K.V. Lakshmi, B.R. Mehta, J.P. Singh, Appl. Phys. Lett. 92 (2008) 171907-1.
[26] M.J. Zheng, L.D. Zhang, G.H. Li, X.Y. Zhang, X.F. Wang, Appl. Phys. Lett. 79 (2001) 839.
[27] G. Wang, J. Park, D. Wexler, M.S. Park, J.H. Ahn, Inorg. Chem. Commun. 46 (2007) 4778.
[28] Y. Li, w. Cai, G. Duan, F. Sun, B. Cao, F. Lu, Q. Fang, I.W. Boyd, Appl. Phys. A 81 (2005) 269.
[29] Y. Zhao, Z. Zhang, Z. Wu, H. Dang, Langmuir 20 (2004) 27.
[30] X.P. Shen, H.J. Liu, X. Fan, Y. Jiang, J.M. Hong, Z. Xu, J. Cryst. Growth 276 (2005) 471.